

Article

Phenomenological 2D and 3D Models of Ductile Fracture for Girth Weld of X80 Pipeline

Naixian Li ¹, Bin Jia ^{1,2,*}, Junhong Chen ³, Ying Sheng ¹ and Songwen Deng ¹

¹ School of Civil Engineering and Architecture, Southwest University of Science and Technology, Mianyang 621010, China

² Shanghai Key Laboratory of Engineering Structure Safety, Shanghai 200032, China

³ Gas Transmission Management Division Southwest Oil, Gasfield Company PetroChina, Chengdu 610041, China

Abstract: Welding is the main method for oil/gas steel pipeline connection, and a large number of girth welds are a weak part of the pipeline. Under extremely complex loads, a steel pipeline undergoes significant plastic deformations and eventually leads to pipeline fracture. A damage mechanics model is a promising approach, capable of describing material fracture problems according to the stress states of the materials. In this study, an uncoupled fracture 2D model with a function of fracture strain and stress triaxiality, two uncoupled 3D fracture models, a consider the effect of Lode parameter stress-modified critical strain (LSMCS) model, and an extended Rice–Tracey (ERT) criterion were applied to X80 pipeline girth welds. Comprehensive experimental research was conducted on different notched specimens, covering a wide range of stress states, and the corresponding finite element models were established. A phenomenon-based hybrid numerical–experimental calibration method was also applied to determine the fracture parameter for these three models, and the stress triaxiality of the influence law of the tensile strength was analyzed. The results showed that the proposed fracture criterion could better characterize the ductile fracture behaviors of the girth welds of the X80 pipeline; however, the prediction accuracy of the 3D fracture model was higher than that of the 2D fracture model. The functional relationship between the tensile strength and stress triaxiality of the X80 pipeline girth welds satisfied the distribution form of the quadratic function and increased monotonically. The research results can be used to predict the fracture of X80 pipeline girth welds under various complex loads.

Keywords: X80 pipeline girth weld; ductile fracture; damage model; tensile strength



Citation: Li, N.; Jia, B.; Chen, J.; Sheng, Y.; Deng, S. Phenomenological 2D and 3D Models of Ductile Fracture for Girth Weld of X80 Pipeline. *Buildings* **2023**, *13*, 283. <https://doi.org/10.3390/buildings13020283>

Academic Editor: Oldrich Sucharda

Received: 23 November 2022

Revised: 10 January 2023

Accepted: 16 January 2023

Published: 18 January 2023



Copyright: © 2023 by the author. Licensee MDPI, Basel, Switzerland. This article is an open access article distributed under the terms and conditions of the Creative Commons Attribution (CC BY) license (<https://creativecommons.org/licenses/by/4.0/>).

1. Introduction

Pipelines made of high-strength steel are the most commonly used means of transporting oil and gas (O&G) for onshore and offshore installations. X80 pipeline steel is widely used for oil and gas pipelines because of its excellent mechanical properties, and its laying quantity is also increasing [1,2]. Given the fixed length of pipes, long-distance natural gas transmission pipelines have to be connected by manual girth welding every 12 m. Owing to several limitations, girth welds inevitably produce defects during the welding process, making them a vulnerable point in pipeline structures. In actual projects, pipelines are laid in a variety of environments, such as mountainous areas, deserts, glaciers, and oceans. When these environments change or a third party carries out construction activities in the vicinity, geological disasters, such as settlement and landslides, can occur in the location of the pipeline. As weak points of the pipelines, girth welds are most likely to be destroyed during these events. Recently, a strain-based method has been developed, which has a better resolution to deal with global plastic deformations, compared with the traditional stress-based method. This method has been applied to standards and recommended practices to evaluate defects in pipes [3–6]. However, it is difficult to capture the

actual failure physics involved in the localized plastic deformation and material tearing in this method [7].

Fracture and damage mechanics theories are commonly employed to study ductile fractures. Both theories require a full understanding of the mechanical properties of materials. Based on 104 experimental results, Khalaj [8,9] realized the prediction of mechanical properties of metal materials through artificial neural networks and successfully predicted the tensile strength of X70 pipeline steel by chemical composition elements. Pouraliakbar [10] used an adaptive neuro-fuzzy interface system (ANFIS) to simulate the Charpy impact energy of Al6061-SiCp laminated nanocomposites prepared by mechanical alloying in two configurations of splitting and crack resistance, which provided a new idea for obtaining the mechanical properties of materials. In traditional fracture mechanics, material fracture toughness data are required, and fracture toughness is considered in terms of the resistance curve. Traditional fracture mechanics generally have certain limitations. First, they must be studied based on material cracks, therefore, prediction of object fractures without prefabricated cracks is impossible. Second, the crack propagation direction, including the crack path deviations, cannot be predicted without a user-defined criterion [11].

However, the damage mechanics theory can describe the initiation and propagation of cracks by allowing damage evolution to include the influences of both local stress and strain variables [11]. Thus, the limitations of traditional fracture mechanics can be effectively removed. The Gurson–Tvergaard–Needleman (GTN) model, based on micromechanics, is a classical coupled damage mechanics model. This model was developed from the porous plastic model developed by Gurson [12] and was used to describe the effect of holes on the plastic behavior of materials. The model was then modified by Tvergaard and Needleman, and the failure process of the materials was expressed by describing the evolution behaviors of the holes [13,14]. However, the original GTN model could not describe the material failure under shear stress. The modified GTN model [15–17] considering shear failure resulted in an increase in the free parameters of the model, which make the calibration difficult. The other model is an uncoupled fracture model that excludes the effect of damage on the mechanical properties of materials, and is the common method used in industry. The uncoupled fracture model typically consists of a mathematical expression based on the relationship between the fracture strain and stress state, forming a fracture criterion. Many uncoupled fracture models, such as Johnson–Cook criterion [18], stress-modified critical strain model [19], Xue–Wierzbicki model [20], and extended Rice–Tracey (ERT) criterion [21], have been developed.

Damage-mechanics models have been widely used for metal fractures [22–24]. Several mechanical damage models have been applied to oil/gas pipelines. Oh [25–28] formulated a series of notch tensile specimens for X65 pipeline steel, developed GTN and uncoupled fracture models, and verified the accuracy of the model through blasting experiments with full-scale pipelines having defects. Shinohara [29] integrated the GTN and Thomason models to develop a fracture model capable of describing the anisotropic fracture behavior of X100 pipeline steel. Paredes [30] calibrated the MMC (Mohr–Coulomb) parameters for X70 pipeline steel. Han [31] calibrated the MMC material parameters versus ERT for X80 pipeline steel, based on experiments. Regarding the research on the ductile fracture of girth welds in oil and gas pipelines, Sarzosa [32] developed the fracture track between the Lode parameter, stress triaxiality, and fracture strain for the girth weld on the X65 pipeline, and the simulated fracture prediction effect was in good agreement with the test results. Although damage models have been frequently applied by many researchers in simulating ductile fractures in pipe steels, the feasibility of these models remains subject to verification, and the calibration of parameters has been controversial. In addition, ductile fracture models for pipeline girth welds are lacking.

In this study, a series of welded tensile specimens, under different stress states, was designed for X80 pipeline girth welds, and a corresponding finite element model was established. The girth-weld fracture parameters of the X80 pipeline under different stress states were determined and obtained through experimental tests and finite element simulations.

A 2D fracture model of the stress triaxial degree and fracture strain was established, and the uncoupled 3D fracture model parameters of an extended Rice–Tracey (ERT) model and the consider the effect of Lode parameter stress-modified critical strain (LSMCS) model were fitted. The established constitutive and fracture models can be used for the safety risk assessment of the girth welds of X80 pipelines.

2. Overview of the Damage Model

2.1. Characterization of Stress States

In previous studies on ductile fracture, stress triaxiality and the Lode parameter has been extensively applied to characterize the stress states of materials and were the two main parameters that affect fracture strain. The stress triaxial with the Lode parameter is expressed as

$$\eta = \frac{\sigma_m}{\bar{\sigma}} \quad (1)$$

$$\bar{\theta} = 1 - \frac{2}{\pi} \arccos \frac{27J_3}{2\bar{\sigma}^3} \quad (2)$$

where η is the stress triaxiality, $\bar{\theta}$ is the dimensionless Lode angle parameter, σ_m is the mean stress, $\bar{\sigma}$ is the equivalent stress, and J_3 is the third invariant of the deviatoric stress.

$$\bar{\sigma} = \sqrt{3J_2} = \sqrt{\frac{1}{2}[(\sigma_1 - \sigma_2)^2 + (\sigma_2 - \sigma_3)^2 + (\sigma_3 - \sigma_1)^2]} \quad (3)$$

$$J_3 = (\sigma_1 - \sigma_m)(\sigma_2 - \sigma_m)(\sigma_3 - \sigma_m) \quad (4)$$

$$\sigma_m = \frac{1}{3}(\sigma_1 + \sigma_2 + \sigma_3) \quad (5)$$

where J_2 is the second invariant of the deviatoric stress and $\sigma_1, \sigma_2, \sigma_3$ denotes the three principal stresses in the stress tensor.

2.2. Uncoupled Fracture Models

2.2.1. Extended Rice–Tracey (ERT) Model

Rice and Tracey studied the growth of isolated spherical voids in an infinite ideal rigid-plastic matrix and developed the well-known Rice–Tracey (RT) fracture criterion [33]. Gruben [21] introduced the influence of the Lode parameters in the RT model using the correction proposed by Nahshon [17] and obtained the ERT model as follows:

$$\bar{\epsilon}_f^{pl} = \frac{1}{R_1 \exp(R_2 \eta) + R_3 \sin^2[\frac{\pi}{2}(1 - \bar{\theta})]} \quad (6)$$

where R_1, R_2, R_3 are three material parameters to be determined, and $\bar{\epsilon}_f^{pl}$ is fracture strain.

2.2.2. Consider the Effect of Lode Parameter Stress-Modified Critical Strain (LSMCS) Model

Based on the stress-modified critical strain model (SMCS), which only considers stress triaxiality on fracture strain, Huang [34] added the influence term of the Lode parameters and developed the LSMCS model as follows:

$$\bar{\epsilon}_f^{pl} = \alpha \exp(-1.5\eta)[\gamma + (1 - \gamma)\bar{\theta}^2] \quad (7)$$

where α, γ are the two material parameters to be determined.

3. Experimental Methods

In this study, the ductile fracture of X80 pipe girth weld is studied by combining test and simulation, and the flow chart is shown in Figure 1. Given that fabricating small-sized tensile specimens for girth welds is difficult, a study was conducted to design

heteromorphic specimens with welded joints. To obtain the fracture parameters of X80 pipeline girth welds, the constitutive model of X80 pipeline steel must be determined. For X80 pipeline steel, standard tensile specimens (smooth round bar: SRB) were designed based on the requirements of GB/T +228.1–2010 [35], as shown in Figure 2. For weld specimens, based on HB 5214–1996 [36], GB/T 7314–2017 [37], and HB 6736–1993 [38], notched round bar tension specimens (radius: 1 mm, 3 mm, 5 mm, NRB1, NRB3, NRB5) and compression and flat shear (FS) specimens were designed. Following a previous study [31], a central-hole tensile specimen (CH6) with a central round hole diameter of 6 mm was designed, as shown in Figure 3. The stress state of high-stress triaxiality was determined using round bar notch weld specimens; low-stress triaxiality was determined using shear weld specimens; negative stress triaxiality was obtained using compression specimens; and the stress state of stress triaxiality near 0.4 was determined using central-hole tensile specimens.

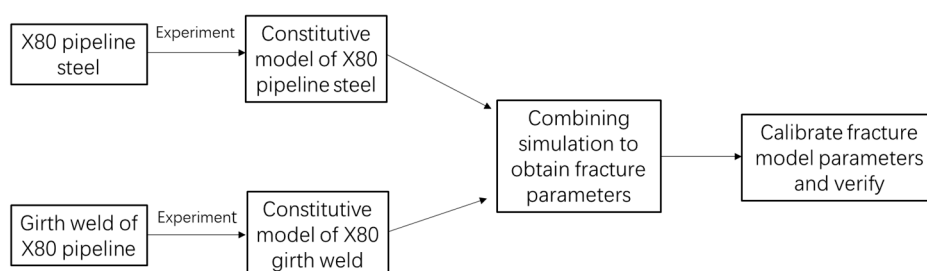


Figure 1. Research flow chart.

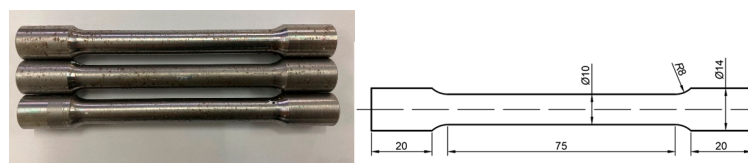


Figure 2. Standard tensile specimen (dimensions in mm).

The experiment was performed using a CMT5150 universal test machine, with a maximum load of 100 kN, manufactured by Meister Industrial System (China) Co., Ltd., in June 2010. The distance of the extensometer was 50 mm, which has a grade 1 accuracy. All the experiments were conducted with a loading rate of 0.45 mm/min. The material used in this research was an X80 girth-weld pipe, with a diameter of 1219 mm and a pipe thickness of 18.4 mm. The welding material was 91T8, and a steel grade can be additionally qualified according to TR/ISO 15608 [39]. The average weld parameters used for preparing the test weld using the FCAW process are (1) welding current 170 Amps; (2) welding voltage 20 V; (3) wire feed speed 5 m/min, and front arc energy 0.72 kJ/mm, while the V Groove and welding were performed in accordance with GB/T 31032-2014 [40], and the welding method according to ISO 4063 [41]. The size of the weld joint is shown in Figure 4. To ensure the quality of the welding, non-destructive testing of the welds was performed; non-destructive testing includes radiographic testing and time of flight diffraction, ensuring that the source of specimen welds without defects. All specimens were obtained from the longitudinal direction of the pipe, and the girth weld was ensured to be located at the notch of the special-shaped specimen, as shown in Figure 5.

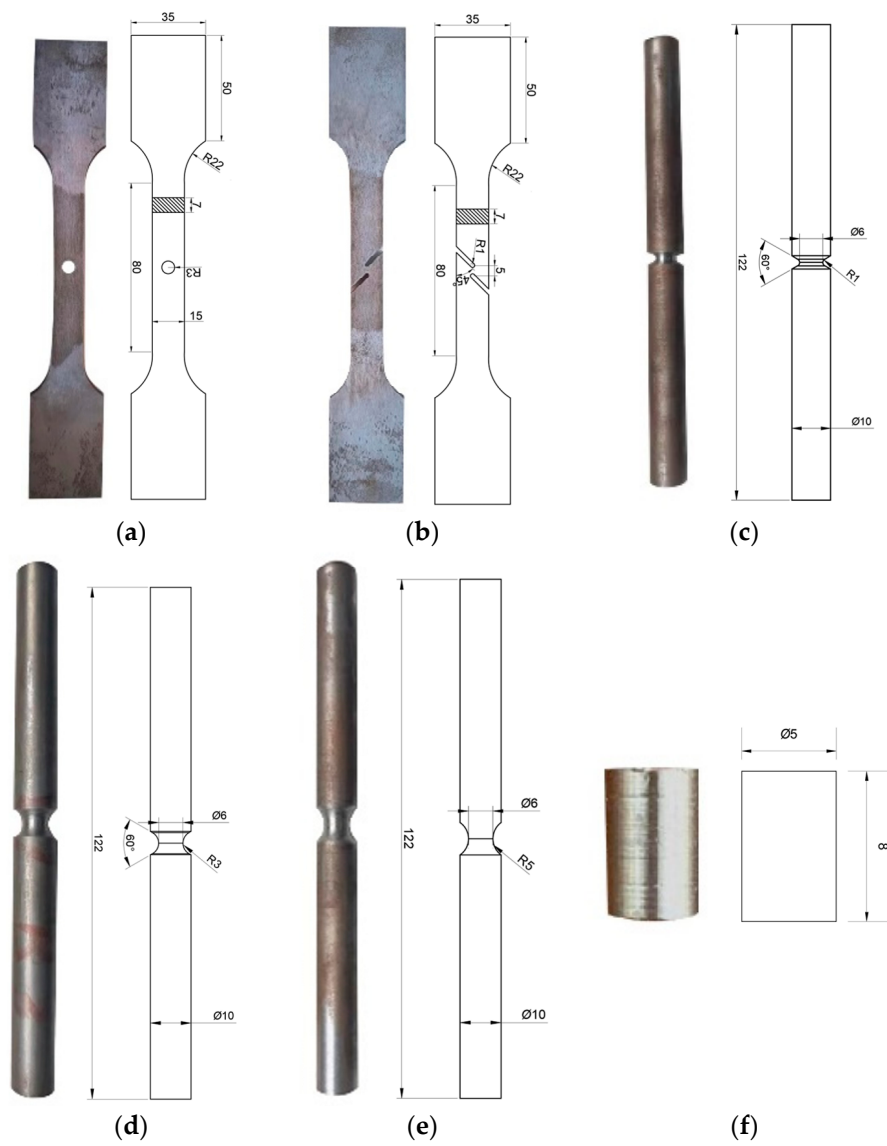


Figure 3. Weld special-shaped specimens (dimensions in mm): (a) CH6, (b) FS, (c) NRB1, (d) NRB3, (e) NRB5, and (f) compression.

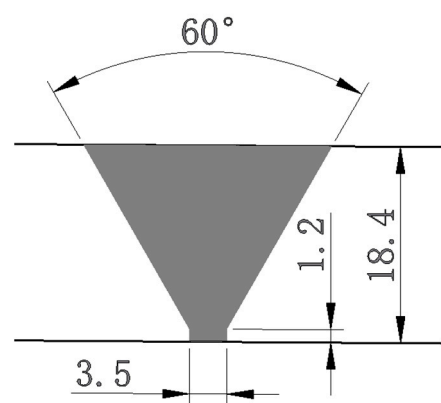


Figure 4. Weld joint (dimensions in mm).

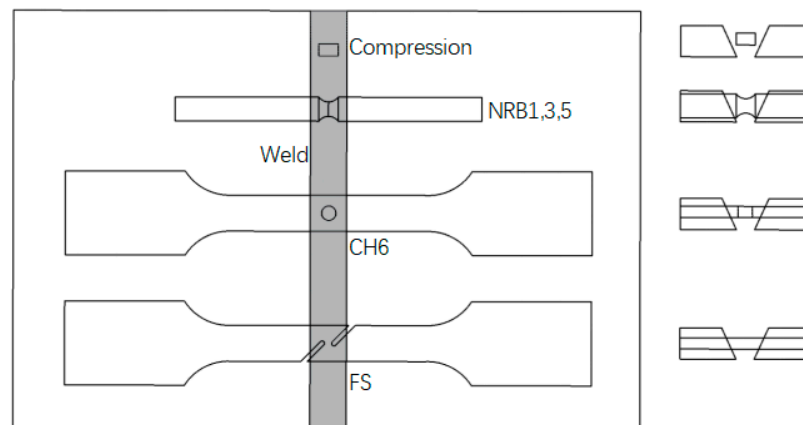


Figure 5. Schematic of weld specimen pick-up.

4. Constitutive Equations

4.1. Constitutive Model of X80 Pipeline Steel

Figure 5 shows the true stress-strain curve of the X80 pipeline steel drawn based on the results of the experiment. It was observed that X80 pipeline steel had no obvious yield plateau; therefore, the stress when 0.2% plastic strain occurred was adopted as the yield strength ($R_{p0.2}$). The mechanical parameters of X80 pipeline steel are summarized in Table 1.

Table 1. Mechanical parameters of X80 pipeline steel.

Young's Modulus (MPa)	Poisson's Ratio	Yield Strength/ $R_{p0.2}$ (MPa)	Tensile Strength (MPa)
206,000	0.3	638	739

Under large strains, the difference in the stress anisotropy of X80 pipeline steel could be ignored [31]; therefore, X80 pipeline steel could be regarded as an isotropic material in this study. For invalid data of specimens after necking, stress-strain data before necking were adopted, and the Johnson–Cook constitutive model was applied to fit the hardening curve which describes the hardening behavior after necking. This parameter is expressed as [42]

$$\bar{\sigma} = \left[A + B(\bar{\epsilon}^{pl})^n \right] \left[1 + C \ln\left(\frac{\dot{\bar{\epsilon}}^{pl}}{\dot{\bar{\epsilon}}_0}\right) \right] (1 - \hat{\theta}^m) \quad (8)$$

where $\bar{\epsilon}^{pl}$ is the equivalent plastic strain, $\frac{\dot{\bar{\epsilon}}^{pl}}{\dot{\bar{\epsilon}}_0}$ is the dimensionless plastic strain rate, $1 - \hat{\theta}^m$ is a temperature-related term, and A, B, C, n, m are parameters to be determined experimentally.

In this study, quasi-static loading was adopted, and the temperature changes of the specimens during loading were ignored. Therefore, the temperature and strain rate terms in Equation (8) were equated to 1, simplifying the equation into

$$\bar{\sigma} = A + B(\bar{\epsilon}^{pl})^n \quad (9)$$

The hardening curve data before neck shrinkage were selected for the preliminary parameter fitting. The load-displacement curve of the standard tensile specimen was drawn using a finite element software and was compared with the experimental results. The slope of the hardening curve after the neck shrinkage was continuously adjusted until the simulation (FEM) results were consistent with the experimental results. Finally, parameters A, B , and n were determined to be 506.94 MPa, 398.467 MPa, and 0.17402, respectively. The hardening curve is shown in Figure 6b, and a comparison of the experimental and finite

element results is shown in Figure 6c. The established constitutive model can characterize the mechanical behavior of X80 pipeline steel.

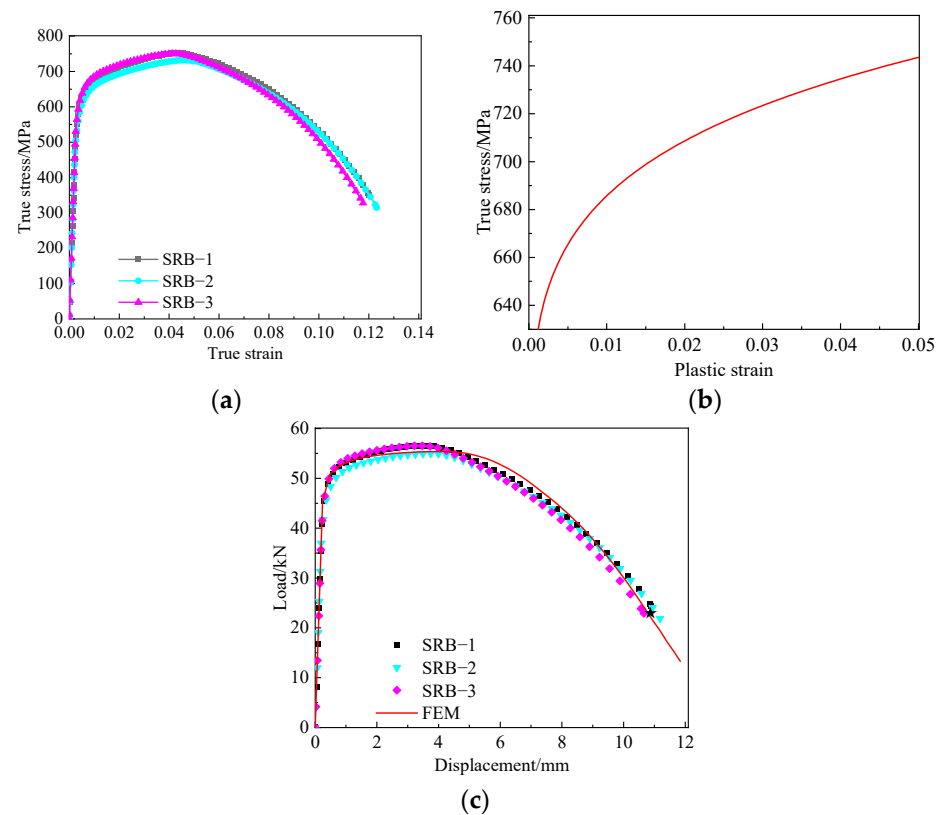


Figure 6. X80 pipeline steel stress-strain curve: (a) true stress-strain curve, (b) Johnson–Cook hardening curve, and (c) comparison of finite element and experimental results.

4.2. Constitutive Model of Girth Weld

According to numerous studies [43–46], the mechanical properties of the elastic stage of a girth weld are consistent with those of the base metal, which was also considered in this work. In this study, the constitutive relationship of the girth weld was determined using compression specimens. Owing to the influence of the friction force at the loading end of the compression machine, the compressed specimens formed obvious “drum shapes”. This shape led to the inaccuracy of the constitutive relationship obtained directly through experiments and the correct hardening constitutive curve of the weld material established with the corresponding finite element model. Finite element software uses ABAQUS2022, and Figure 7 shows the finite element model of the compression specimens. Two rigid plates were set up in which the bottom plate was completely fixed, the upper plate was loaded with a downward displacement, the friction coefficient (μ) between the rigid body presses and the specimens was set to 0.15, and the mesh size was 0.2, totaling into 25,600 elements. The quasi-static calculation was carried out using the C3D8R solid element and explicit dynamics (the kinetic energy proportion was less than 5% of the internal energy). The constitutive curve was constantly corrected using the finite element software, verifying until it was consistent with the experimental conditions. The final plastic hardening constitutive curve of the X80 girth weld is shown in Figure 8a, and Figure 8b shows the comparison results between test and finite element model (FEM). The hardening constitutive model finally determined can well reflect the mechanics of materials and uses a piecewise function description of

$$\begin{cases} \bar{\sigma} = 490.2 + 478.1(\bar{\epsilon}^{Pl})^{0.1918} (0 < \bar{\epsilon}^{Pl} < 0.272) \\ \bar{\sigma} = 120\bar{\epsilon}^{Pl} + 829 (0.272 < \bar{\epsilon}^{Pl}) \end{cases} \quad (10)$$

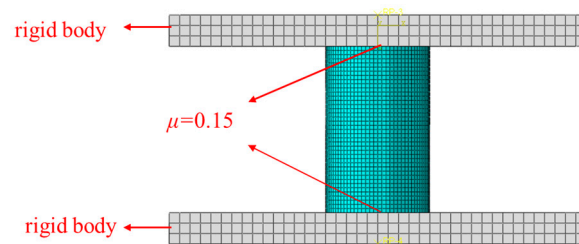


Figure 7. Compressed specimen loading model.

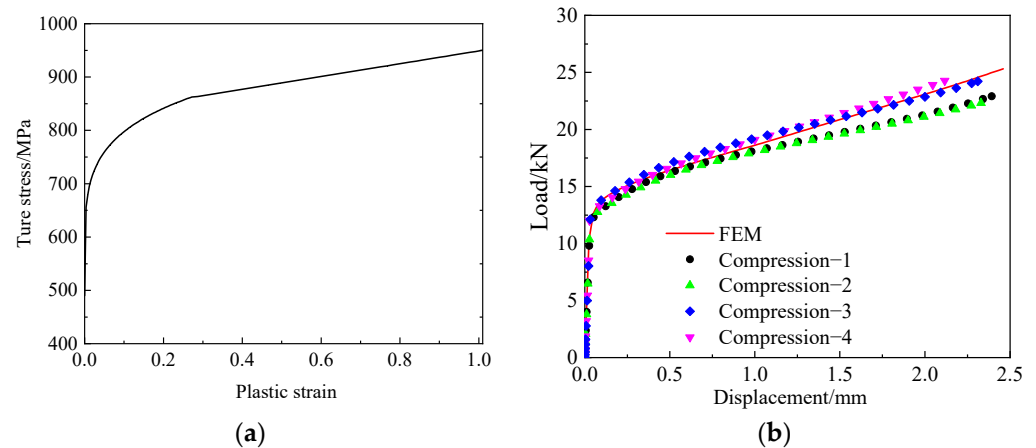


Figure 8. X80 girth weld constitutive model: (a) hardening curve; (b) comparison of test results with FEM.

5. Calibration Procedure

5.1. Finite Element Model

The fracture strain, stress triaxiality, and Lode parameters of the test specimens were analyzed and calibrated according to the elastic-plastic finite element model. ABAQUS was used to establish a three-dimensional finite element model of the special-shaped notch tensile specimen to obtain the simulated load displacement curves. A large deformation was observed at the weld gap, and its heat-affected zone was either still in the elastic stage or the plastic stage was small and could be neglected, therefore, the material softening of the heat-affected zone could be assumed negligible. The notch position was endowed with the attributes of the weld material, and the weld was considered to be an isotropic uniform material [47]. One end of the specimen was articulated, and the other end was loaded with displacement, as shown in Figure 9. C3D8R solid elements were used for all specimens. The global element size was 1mm, the notch part was encrypted, the CH6 and FS middle densified element size was 0.2, while the element of the notch part of the round bar specimen was densified along the longitudinal direction and the element size was 0.2 mm. Calculate using explicit dynamics (the kinetic energy proportion is less than 5% of the internal energy) and reduce integral control.

It was seen from the load displacement curves drawn based on the finite element and experimental results shown in Figure 10 that the established base material and girth weld constitutive models could reflect the mechanical behaviors of the weld tensile specimens under different stress states. The initial fracture points of the specimens are marked with “★” on their respective curves in Figure 10. The experimental results revealed notched round bar cracks at the specimen center and plate-pattern cracks on the notched surface. The critical element determined by each specimen is shown in Figure 10. The equivalent plastic strain of the critical element under the state of fracture displacement is the fracture strain. The maximum load simulation value of NRB3 was slightly higher than the test value, which may be caused by the mechanical non-uniformity of the weld. However, according to the simulation of all test specimens, it is reasonable to regard the weld as isotropic. The

element body at the fracture position was selected to evaluate the evolution processes of the stress triaxiality, Lode parameters, and equivalent plastic strain, as illustrated in Figure 11. The Lode parameter of the round bar specimen was constant at 1. It was found that the round-hole plate in the process of tensile change was not near 0.5, and the shear specimen remained near 0. In addition, the stress triaxiality of the sheet metal remained unchanged during the tensile process, whereas those of the notched round bar tensile specimens all increased to different levels, and the stress triaxiality of the specimens with 1 mm radius was increased significantly.

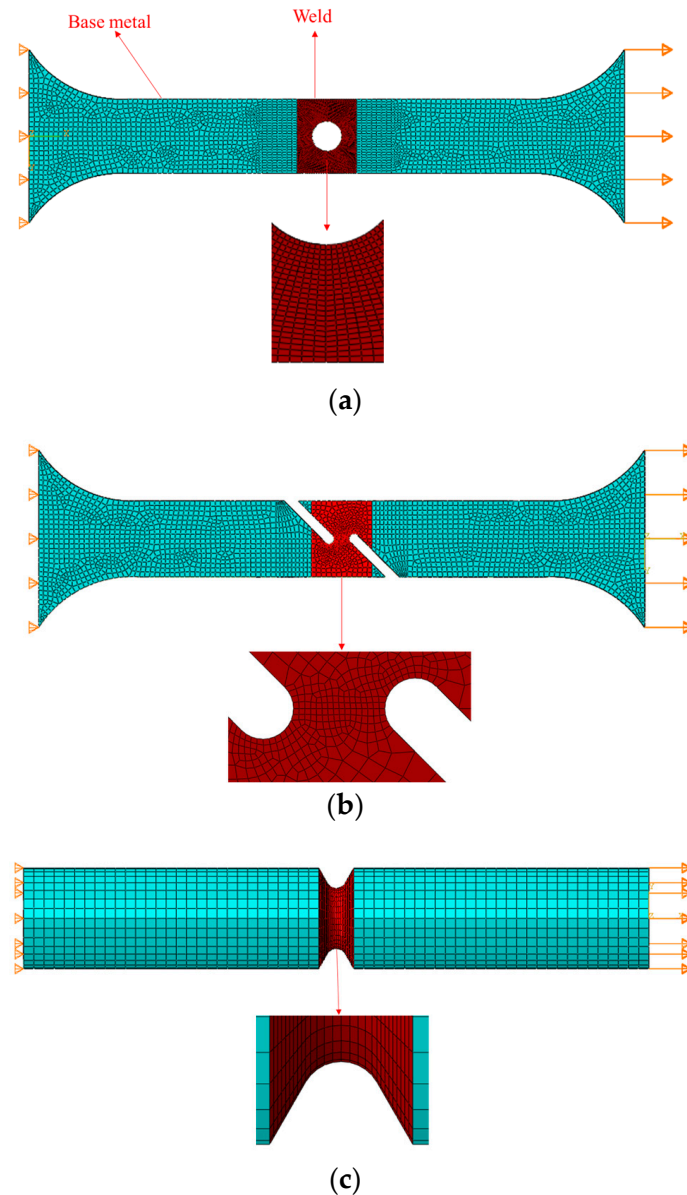


Figure 9. Cont.

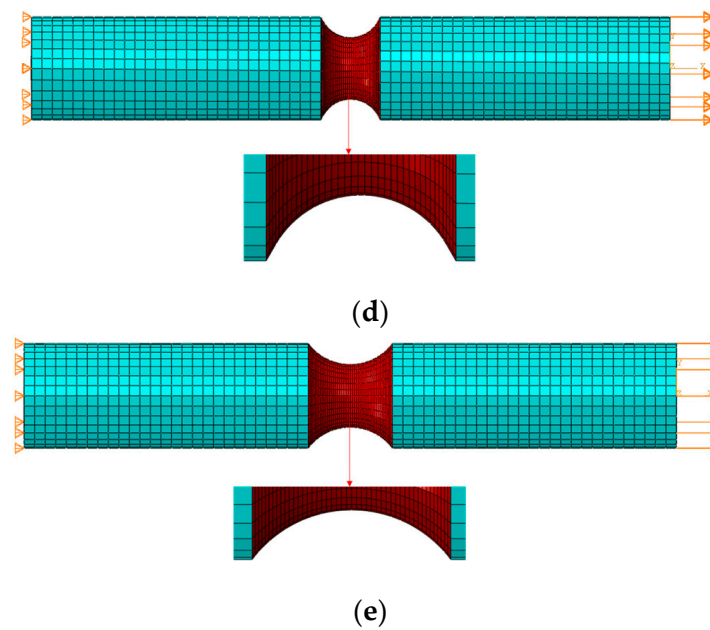


Figure 9. Finite element mesh models: (a) CH6; (b) FS; (c) NRB1; (d) NRB3; (e) NRB5.

5.2. Fitting of Experiment Data

The stress states of the specimens constantly changed during the entire tensile process; therefore, the stress triaxiality of the element had to be averaged with the Lode parameters as follows [48,49]:

$$(\eta)_{av} = \frac{1}{\bar{\epsilon}_f^{pl}} \int_0^{\bar{\epsilon}_f^{pl}} \eta d\bar{\epsilon}^{pl} \tag{11}$$

$$(\bar{\theta})_{av} = \frac{1}{\bar{\epsilon}_f^{pl}} \int_0^{\bar{\epsilon}_f^{pl}} \bar{\theta} d\bar{\epsilon}^{pl} \tag{12}$$

where $(\eta)_{av}$ denotes the average stress triaxiality, and $(\bar{\theta})_{av}$ denotes the average Lode parameter.

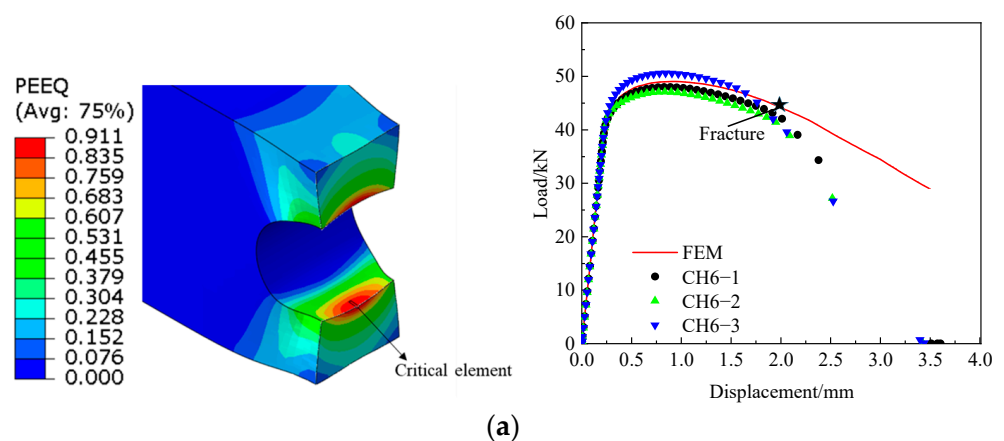


Figure 10. Cont.

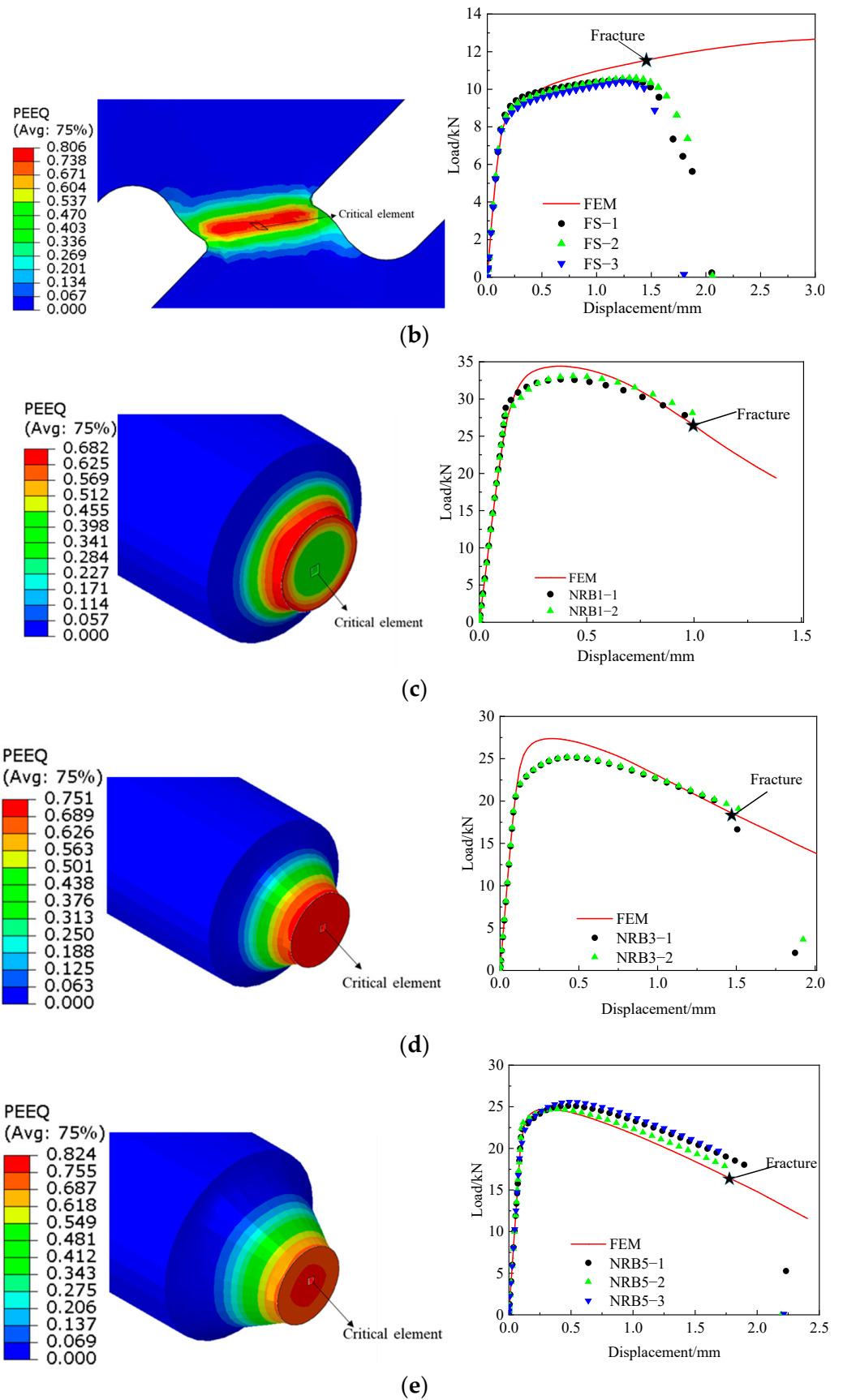


Figure 10. Determination of critical displacement: (a) CH6; (b) FS; (c) NRB1; (d) NRB3; (e) NRB5.

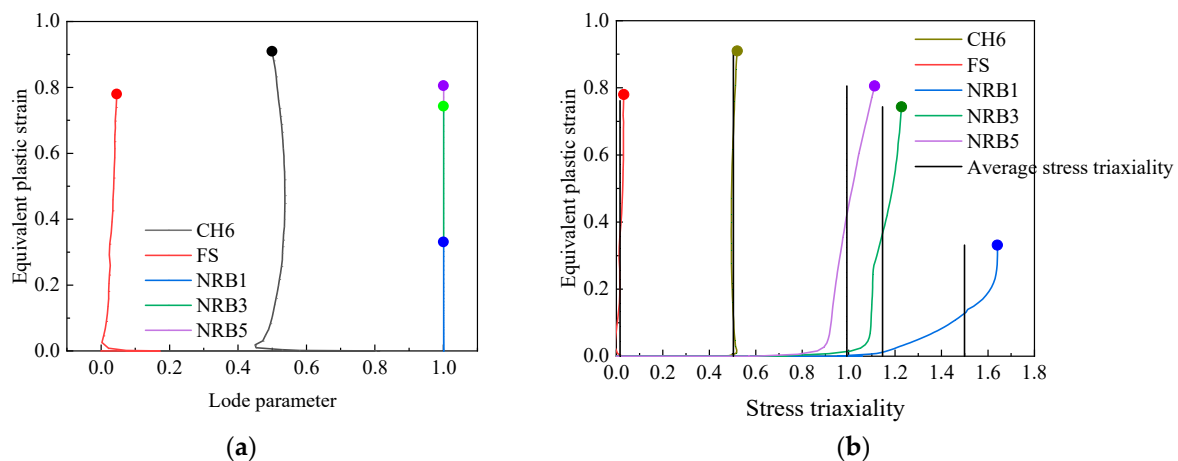


Figure 11. Evolution of equivalent plastic strain and stress states: (a) evolution of equivalent plastic strain and Lode parameters; and (b) evolution of equivalent plastic strain and stress triaxiality.

5.2.1. Fitting of 2D Fracture Criteria

By neglecting the effects of the Lode parameters on the fracture strain, the fracture criterion was expressed as a function of the stress triaxiality and fracture strain. The Johnson–Cook failure model presented a good fracture prediction model for materials under high-stress triaxiality. In this study, the Johnson–Cook failure model was adopted to determine the relationship between fracture strain and stress triaxiality under high stress triaxiality, as follows [18]:

$$\bar{\epsilon}_f^{pl} = [d_1 + d_2 \exp(d_3 \eta)] \left[1 + d_4 \ln\left(\frac{\dot{\epsilon}^{pl}}{\dot{\epsilon}_0}\right) \right] (1 + d_5 \hat{\theta}^m) \quad (13)$$

where $d_1 - d_5$ are parameters to be determined by experiment, and $(1 + d_5 \hat{\theta}^m)$ is a temperature-related term.

Quasi-static loading was applied in this study, and the temperature changes in the specimens during loading were ignored. Therefore, the temperature and strain rate terms in Equation (13) were eliminated, which simplifies it to

$$\bar{\epsilon}_f^{pl} = d_1 + d_2 \exp(d_3 \eta) \quad (14)$$

The average stress triaxiality and fracture strain values determined above are summarized in Table 2. Based on the presented data, a failure model function of the girth weld of the X80 pipeline was developed. The Johnson–Cook failure model was applied to fit the round-hole tensile and notch specimens. The fracture strain at a stress triaxiality of 0.333 was determined by extension, which was described by a linear function for the shear specimen, and the fracture strain when the stress triaxiality was 0 was determined by linear function extension.

Table 2. Average stress triaxiality, Lode parameter, and fracture strain of each specimen.

	NRB1	NRB3	NRB5	CH6	FS
Average stress triaxiality	1.498	1.146	0.992	0.503	0.019
Average Lode parameter	1	1	1	0.521	0.031
Fracture strain	0.331	0.743	0.806	0.910	0.780

Bao [50] obtained the fracture cutoff effect of materials; that is, when the stress triaxiality of the material is $-1/3$, the fracture strain tends to approach infinite at this point. No cracks were observed in the specimens during the compression experiments. Therefore, a fracture strain equal to 5 was used to characterize the uncracked specimens when the

stress triaxiality was $-1/3$. The power function was applied to describe the fracture strain when the stress triaxiality was $-1/3$ to 0 , as stated in Equation (15). The established failure model is illustrated in Figure 12.

$$\begin{cases} \bar{\epsilon}_f^{pl} = -0.6686 + 2.016 \exp(-0.4175\eta) (0.333 < \eta < 1.5) \\ \bar{\epsilon}_f^{pl} = 1.052\eta + 0.7346 (0 < \eta < 0.333) \\ \bar{\epsilon}_f^{pl} = \frac{1}{0.4918+\eta} - 1.299 (-0.333 < \eta < 0) \end{cases} \quad (15)$$

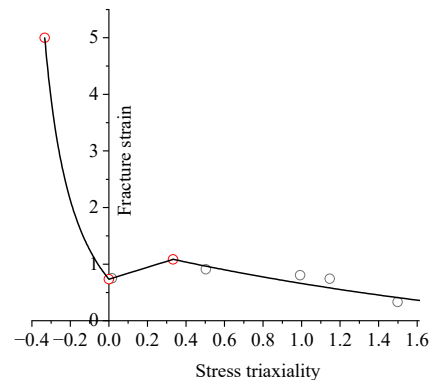


Figure 12. 2D fracture model.

It can be seen from Figure 12 that the monotonic and functional types of the fracture strain curve, at different stress triaxiality intervals, are different. In the stress triaxiality range of $-1/3-0$, the fracture strain function presented a power function distribution and monotonically decreased. From 0 to 0.333 , the function monotonically increases into a linear function. In the range $0.333-1.5$, the function distribution conformed to the Johnson–Cook failure model and decreased monotonically.

5.2.2. Determination of 3D Fracture Model

While considering the Lode parameters in the fracture model, a 3D model is developed in which the stress triaxiality and Lode parameters affect the fracture strain. Equations (6) and (7) were fitted based on the data in Table 2 to determine the unknown parameters in these equations. The resulting fracture model is illustrated in Figure 13 and the determined parameters are summarized in Table 3.

As shown in Figure 13, the ERT and LSMCS models exhibit the same trends in the overall distribution. Under certain Lode parameters, the fracture strain decreased along with an increase in the stress triaxiality. However, slight numerical differences were observed between the two models, mainly in the peak distribution of the fracture strain.

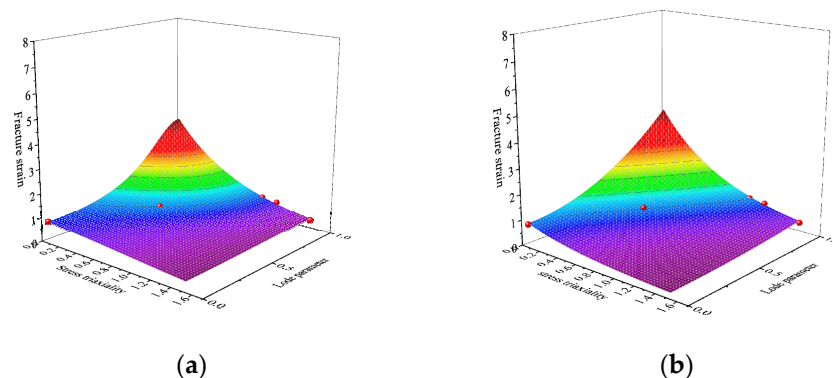


Figure 13. 3D fracture model: (a) ERT and (b) LSMCS.

Table 3. Determined model parameters.

ERT			LSMCS	
R_1	R_2	R_3	α	γ
0.279	1.477	1.030	3.883	0.218

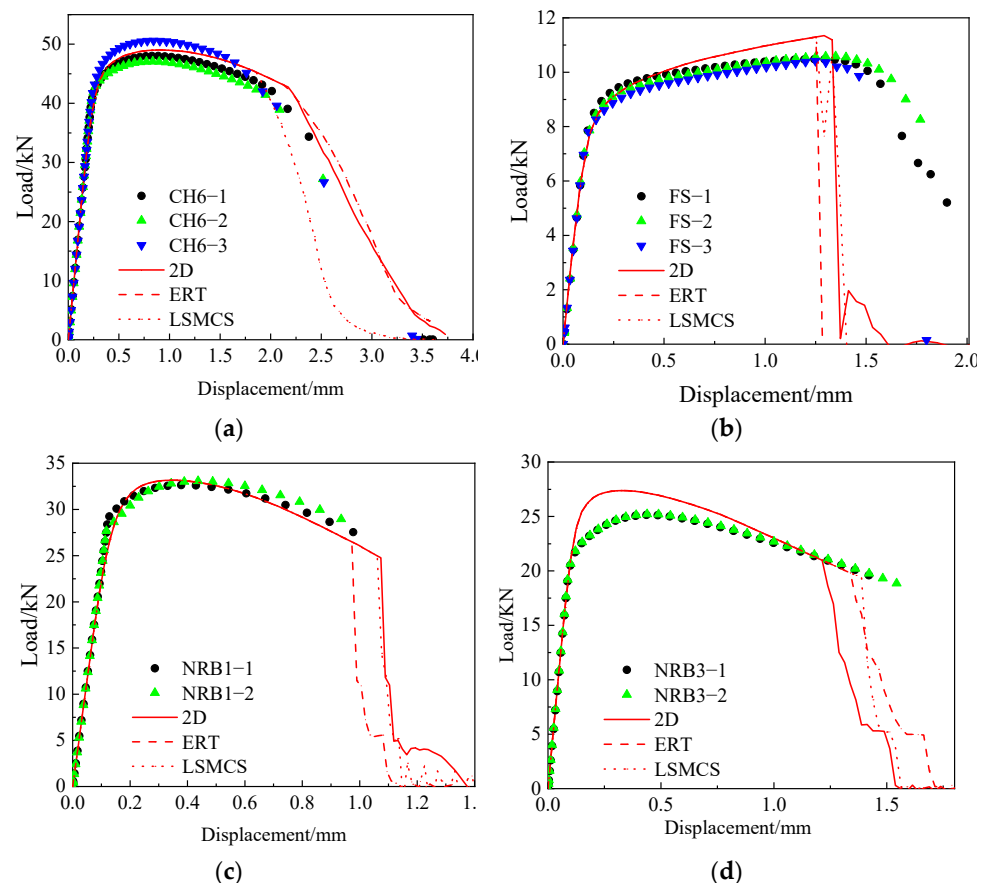
6. Comparison with Notched Tensile Specimen Experiments

To verify the accuracy of the established girth weld failure model for X80 pipelines, a failure model was introduced using ABAQUS to conduct a fracture simulation of the experimental processes mentioned above. Several points on the function of the 2D model were selected using the built-in ductile damage of ABAQUS. The 3D model defined the functional relationship between stress triaxiality, Lode parameters, and fracture strain through the keywords in the INPUT file provided by ABAQUS, which defined the correlation between the Lode angle function and fracture strain. The conversion relationship between the Lode angle function and Lode angle parameters is as follows:

$$\bar{\theta} = 1 - \frac{2}{\pi} \arccos(\zeta) \quad (16)$$

where ζ is the Lode angle function.

The simulation results are shown in Figure 14. It was observed that the fracture model that considered the influences of the Lode parameters was significantly superior to the 2D model. The maximum error between the simulated crack initiation displacement and the average experimental crack initiation displacement of the 2D fracture model was 18%, and that of the 3D fracture model was less than 10%. Figure 15 is a comparison of experimental and simulated fracture morphology, and the fracture morphology is basically consistent.

**Figure 14.** Cont.

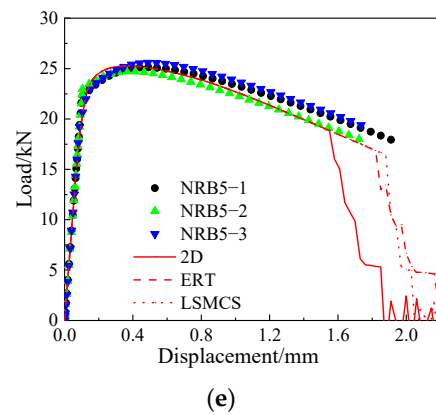


Figure 14. Comparison between finite element and experimental fracture: (a) CH6, (b) FS, (c) NRB1, (d) NRB3, and (e) NRB5.

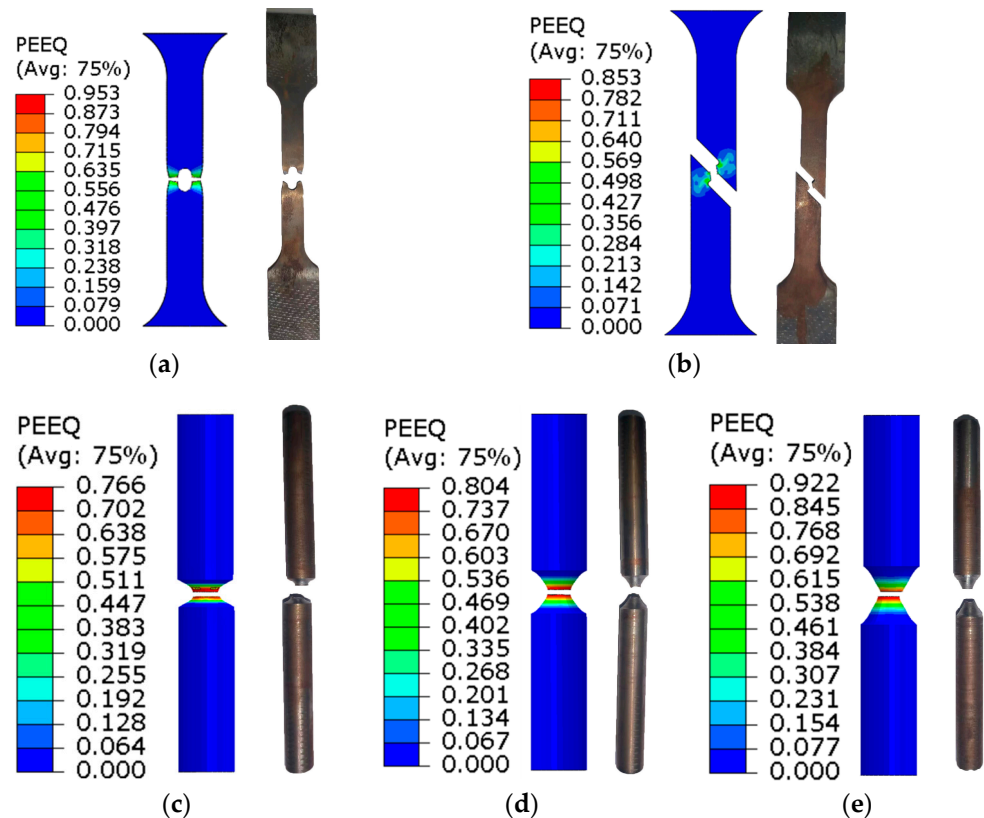


Figure 15. Comparison of experimental and simulated fracture morphology: (a) CH6, (b) FS, (c) NRB1, (d) NRB3, and (e) NRB5.

7. Influence of Stress Triaxiality on Tensile Strength

As shown in Figure 11, the stress triaxiality of each tensile specimen exhibited a constantly increasing trend during the tensile process; thus, the average stress triaxiality was applied to describe the relationship between the stress triaxiality and tensile strength. HB 5214-96 defines notch tensile strength as the maximum load divided by the minimum initial cross-sectional area. The fracture displacement decreased, indicating that ductility decreased with an increase in stress triaxiality. The average value of the tensile strength of the specimen was equated to the tensile strength under each working condition. The determined tensile strength is listed in Table 4, and it can be seen from Figure 16 that the

tensile strength increased with an increase in stress triaxiality [51–53]. The relationship between the average stress triaxiality and ultimate tensile strength is expressed as

$$\sigma_{\text{tensile}} = 506.023(\eta)_{\text{av}}^2 - 622.018(\eta)_{\text{av}} + 956.467 \quad (17)$$

Table 4. Average stress triaxiality and tensile strength of notched specimens.

	NRB1	NRB3	NRB5	CH6
Average stress triaxiality	1.498	1.146	0.992	0.503
Average tensile strength (MPa)	1162	891.1	889.8	770.9
Fracture displacement (mm)	1.000	1.460	1.760	2.070

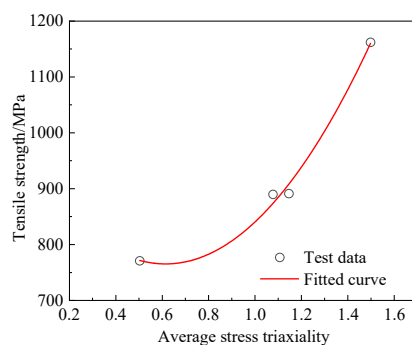


Figure 16. Function relationship between tensile strength and average stress triaxiality.

8. Conclusions

In this study, the ductile fracture of X80 pipeline girth weld was studied experimentally and numerically. The mechanical properties of base metal and weld were obtained through experiments, and the fracture parameters of weld under different stress states were obtained through special-shaped specimens. An uncoupled 2D fracture model and two uncoupled 3D fracture models of the X80 pipeline girth welds were introduced through a phenomenological approach. The 2D model is a function of fracture strain and stress triaxiality. The 3D models were a consider the effect of Lode parameter stress-modified critical strain (LSMCS) model and the extended Rice–Tracey (ERT) criterion.

Tensile failure tests under five different stress states were carried out and corresponding finite element models were established. Fracture parameters from high stress triaxiality to low stress triaxiality were obtained by combining test and numerical simulation. Fracture strain and stress triaxiality were obtained to develop a 2D fracture model. Based on the 2D model, the related parameters of ERT and LSMCS are calibrated considering the influence of the Lode parameters. In addition, a simulation proved the validity of the developed fracture model.

Compared with the 2D fracture models, the 3D fracture models yielded more accurate prediction results. In the fracture prediction of the CH6 and FS specimens, the 2D and 3D fracture models provided good prediction results for the fracture displacement. However, in the fracture prediction of the round bar notch specimens, the 2D fracture model generated results in which the fracture displacement was larger or smaller, but the 3D fracture model generated consistently good test results.

The influence of stress triaxiality of weld materials on tensile strength is similar to that of metal materials previously studied, the functional relationship between the tensile strength and stress triaxiality of the X80 pipeline girth welds satisfied the distribution form of the quadratic function and increased monotonically. Ductility decreases with an increase in stress triaxiality.

The research results can be used to predict the fracture of X80 pipeline girth weld under various complex loads, and can be used to evaluate the safety of pipeline girth weld in practical projects.

Author Contributions: N.L.: software, data curation, methodology, writing—original draft preparation. B.J.: conceptualization, resources, supervision. J.C.: writing—review & editing, investigation. Y.S.: formal analysis. S.D.: software. All authors have read and agreed to the published version of the manuscript.

Funding: This research was funded by Natural Science Foundation of Sichuan Province (2022NS-FSC0317), the Open Fund of Shanghai Key Laboratory of Engineering Structure Safety (No. 2019-KF04), Sichuan Provincial Science and Technology Department Project (2020JDTD0021, 2023NS-FSC0887) and National Natural Science Foundation of China (51908476). And the APC was funded by Bin Jia.

Data Availability Statement: The data used in the study is available with the authors and can be shared upon reasonable request.

Conflicts of Interest: The authors declare that they have no known competing financial interests or personal relationships that could have appeared to influence the work reported in this paper.

References

1. Witek, M. Possibilities of Using X80, X100, X120 High-Strength Steels for Onshore Gas Transmission Pipelines. *J. Nat. Gas Sci. Eng.* **2015**, *27*, 374–384. [[CrossRef](#)]
2. American Petroleum Institute. *Specification for Line Pipe, API Specification 5L*; American Petroleum Institute: Washington, DC, USA, 2018; Volume 46.
3. *British Standard BS 7910*; Guide to Methods for Assessing the Acceptability of Flaws in Metallic Structures. BSI Standards Publication: London, UK, 2013.
4. *API 579-2000*; API Recommended Practice 579. Fitness for Service. API Standards. American Petroleum Institute: Washington, DC, USA, 2000.
5. Kocak, M.; Webster, S.; Janosch, J.J.; Ainsworth, R.A.; Koers, R. *FITNET Fitness-for-Service (FFS) Procedure*; GKSS Research Centre Geesthacht: Geesthacht, Germany, 2008.
6. Milne, I.; Ainsworth, R.A.; Dowling, A.R.; Stewart, A.T. Assessment of the Integrity of Structures Containing Defects. *Int. J. Press. Vessel. Pip.* **1988**, *32*, 3–104. [[CrossRef](#)]
7. Fairchild, D.P.; Crapps, J.M.; Cheng, W.; Tang, H.; Shafrova, S. Full-Scale Pipe Strain Test Quality and Safety Factor Determination for Strain-Based Engineering Critical Assessment. In Proceedings of the 2016 11th International Pipeline Conference, Calgary, AB, Canada, 26–30 September 2016; Volume 2.
8. Khalaj, G.; Nazari, A.; Pouraliakbar, H. Prediction of Martensite Fraction of Microalloyed Steel by Artificial Neural Networks. *Neural Netw. World* **2013**, *13*, 117–130.
9. Khalaj, G.; Azimzadegan, T.; Khoeyini, M.; Etaat, M. Artificial Neural Networks Application to Predict the Ultimate Tensile Strength of X70 Pipeline Steels. *Neural Comput. Appl.* **2013**, *23*, 2301–2308. [[CrossRef](#)]
10. Pouraliakbar, H.; Nazari, A.; Fataei, P.; Livary, A.K.; Jandaghi, M. Predicting Charpy Impact Energy of Al6061/SiCp Laminated Nanocomposites in Crack Divider and Crack Arrester Forms. *Ceram. Int.* **2013**, *39*, 6099–6106. [[CrossRef](#)]
11. Kofiani, K.; Nonn, A.; Wierzbicki, T. New Calibration Method for High and Low Triaxiality and Validation OnSENT Specimens of API X70. *Int. J. Press. Vessel. Pip.* **2013**, *111*, 187–201. [[CrossRef](#)]
12. Gurson, A.L. Continuum Theory of Ductile Rupture by Void Nucleation and Growth: Part 1—Yield Criteria and Flow Rules for Porous Ductile Media. *J. Eng. Mater. Technol. Trans. ASME* **1977**, *99*, 2–15. [[CrossRef](#)]
13. Tvergaard, V. On Localization in Ductile Materials Containing Spherical Voids. *Int. J. Fract.* **1982**, *18*, 237–252. [[CrossRef](#)]
14. Tvergaard, V.; Needleman, A. Analysis of the Cup-Cone Fracture in a Round Tensile Bar. *Acta Metall.* **1984**, *32*, 157–169. [[CrossRef](#)]
15. Nielsen, K.L.; Tvergaard, V. Failure by Void Coalescence in Metallic Materials Containing Primary and Secondary Voids Subject to Intense Shearing. *Int. J. Solids Struct.* **2011**, *48*, 1255–1267. [[CrossRef](#)]
16. Jackiewicz, J. Use of a Modified Gurson Model Approach for the Simulation of Ductile Fracture by Growth and Coalescence of Microvoids under Low, Medium and High Stress Triaxiality Loadings. *Eng. Fract. Mech.* **2011**, *78*, 487–502. [[CrossRef](#)]
17. Nahshon, K.; Hutchinson, J.W. Modification of the Gurson Model for Shear Failure. *Eur. J. Mech. A/Solids* **2008**, *27*, 1–17. [[CrossRef](#)]
18. Johnson, G.R.; Cook, W.H. Fracture Characteristics of Three Metals Subjected to Various Strains, Strain Rates, Temperatures and Pressures. *Eng. Fract. Mech.* **1985**, *21*, 31–48. [[CrossRef](#)]
19. Chi, W.-M.; Kanvinde, A.M.; Deierlein, G.G. Prediction of Ductile Fracture in Steel Connections Using SMCS Criterion. *J. Struct. Eng.* **2006**, *132*, 171–181. [[CrossRef](#)]
20. Wierzbicki, T.; Bao, Y.; Lee, Y.W.; Bai, Y. Calibration and Evaluation of Seven Fracture Models. *Int. J. Mech. Sci.* **2005**, *47*, 719–743. [[CrossRef](#)]
21. Gruben, G.; Hopperstad, O.S.; Borvik, T. Evaluation of Uncoupled Ductile Fracture Criteria for the Dual-Phase Steel Docol 600DL. *Int. J. Mech. Sci.* **2012**, *62*, 133–146. [[CrossRef](#)]

22. Zhang, Y.; Liu, Y.; Yang, F. Ductile Fracture Modelling of Steel Plates under Tensile and Shear Dominated States. *J. Constr. Steel Res.* **2022**, *197*, 107469. [[CrossRef](#)]
23. Kacem, A.; Laurent, H.; Thuillier, S. Experimental and Numerical Investigation of Ductile Fracture for AA6061-T6 Sheets at Room and Elevated Temperatures. *Int. J. Mech. Sci.* **2022**, *222*, 107201. [[CrossRef](#)]
24. Zhang, Y.; Shen, F.; Zheng, J.; Münstermann, S.; Li, T.; Han, W.; Huang, S. Ductility Prediction of HPDC Aluminum Alloy Using a Probabilistic Ductile Fracture Model. *Theor. Appl. Fract. Mech.* **2022**, *119*, 103381. [[CrossRef](#)]
25. Oh, C.K.; Kim, Y.J.; Baek, J.H.; Kim, Y.P.; Kim, W.S. Ductile Failure Analysis of API X65 Pipes with Notch-Type Defects Using a Local Fracture Criterion. *Int. J. Press. Vessel. Pip.* **2007**, *84*, 512–525. [[CrossRef](#)]
26. Oh, C.K.; Kim, Y.J.; Baek, J.H.; Kim, W.S. Development of Stress-Modified Fracture Strain for Ductile Failure of API X65 Steel. *Int. J. Fract.* **2007**, *143*, 119–133. [[CrossRef](#)]
27. Oh, C.K.; Kim, Y.J.; Baek, J.H.; Kim, Y.P.; Kim, W. A Phenomenological Model of Ductile Fracture for API X65 Steel. *Int. J. Mech. Sci.* **2007**, *49*, 1399–1412. [[CrossRef](#)]
28. Oh, C.S.; Kim, N.H.; Kim, Y.J.; Baek, J.H.; Kim, Y.P.; Kim, W.S. A Finite Element Ductile Failure Simulation Method Using Stress-Modified Fracture Strain Model. *Eng. Fract. Mech.* **2011**, *78*, 124–137. [[CrossRef](#)]
29. Shinohara, Y.; Madi, Y.; Besson, J. Anisotropic Ductile Failure of a High-Strength Line Pipe Steel. *Int. J. Fract.* **2016**, *197*, 127–145. [[CrossRef](#)]
30. Paredes, M.; Wierzbicki, T.; Zelenak, P. Prediction of Crack Initiation and Propagation in X70 Pipeline Steels. *Eng. Fract. Mech.* **2016**, *168*, 92–111. [[CrossRef](#)]
31. Han, P.; Cheng, P.; Yuan, S.; Bai, Y. Characterization of Ductile Fracture Criterion for API X80 Pipeline Steel Based on a Phenomenological Approach. *Thin-Walled Struct.* **2021**, *164*, 107254. [[CrossRef](#)]
32. Sarzosa, D.F.; Paredes, M.; Savioli, R.; Ruggieri, C.; Leite, L.G.; da Silva, N.S.; Garmbis, A.G. Experimental and Numerical Study on the Ductile Fracture Response of X65 Girth-Welded Joint Made of Inconel 625 Alloy. *Theor. Appl. Fract. Mech.* **2022**, *121*, 103533. [[CrossRef](#)]
33. Rice, J.R.; Tracey, D.M. On the Ductile Enlargement of Voids in Triaxial Stress Fields. *J. Mech. Phys. Solids* **1969**, *17*, 201–217. [[CrossRef](#)]
34. Huang, X.; Zhao, W.; Zhao, J.; Wang, Z. Fracture Model of Q235B Steel Considering the Influence of Stress Triaxiality and Lode Parameter. *J. Basic Sci. Eng.* **2019**, *27*, 1172–1187. (In Chinese) [[CrossRef](#)]
35. GB/T 228.1-2010; Metallic Materials-Tensile Testing-Part 1: Method of Test at Room Temperature. Standardization Administration of the People's Republic of China (SAC): Beijing, China, 2010.
36. HB 5214-1996; Method of Notch Tensile Test for Metals at Room Temperature. Aviation Industry Corporation of China: Beijing, China, 1996.
37. GB/T 7314-2017; Metallic Materials-Compression Test Method at Room Temperature. Standardization Administration of the People's Republic of China (SAC): Beijing, China, 2017.
38. HB 6736-1993; Shear Test Method for Sheet Metal. Aviation Industry Corporation of China: Beijing, China, 1993.
39. ISO/TR 15608; Welding—Guidelines for a metallic materials grouping system. European Committee for Standardization (CEN): Brussels, Belgium, 2006.
40. GB/T 31032-2014; Welding and Acceptance Standard for Steel Pipings and Pipelines. Standardization Administration of the People's Republic of China (SAC): Beijing, China, 2014.
41. SS-EN ISO 4063; 2010 Welding and Allied Processes—Nomenclature of Processes and Reference Numbers. European Committee for Standardization (CEN): Brussels, Belgium, 2012.
42. Johnson, G.R.; Cook, W.H. A Constitutive Model and Data for Metals Subjected to Large Strains, High Strain Rates and High Temperatures. In Proceedings of the 7th International Symposium on Ballistics, The Hague, The Netherlands, 19–21 April 1983; Volume 547.
43. Bastola, A.; Wang, J.; Shitamoto, H.; Mirzaee-Sisan, A.; Hamada, M.; Hisamune, N. Full- and Small-Scale Tests on Strain Capacity of X80 Seamless Pipes. *Procedia Struct. Integr.* **2016**, *2*, 1894–1903. [[CrossRef](#)]
44. Nie, H.; Ma, W.; Xue, K.; Ren, J.; Dang, W.; Wang, K.; Cao, J.; Yao, T.; Liang, X. A Novel Test Method for Mechanical Properties of Characteristic Zones of Girth Welds. *Int. J. Press. Vessel. Pip.* **2021**, *194*, 104533. [[CrossRef](#)]
45. Wu, X.; Shuai, J.; Xu, K.; Lv, Z.; Shan, K. Determination of Local True Stress-Strain Response of X80 and Q235 Girth-Welded Joints Based on Digital Image Correlation and Numerical Simulation. *Int. J. Press. Vessel. Pip.* **2020**, *188*, 104232. [[CrossRef](#)]
46. Zhang, Y.; Shuai, J.; Ren, W.; Lv, Z. Investigation of the Tensile Strain Response of the Girth Weld of High-Strength Steel Pipeline. *J. Constr. Steel Res.* **2022**, *188*, 107047. [[CrossRef](#)]
47. Li, Y.J.; Li, Q.; Wu, A.P.; Ma, N.X.; Wang, G.Q.; Murakawa, H.; Yan, D.Y.; Wu, H.Q. Determination of Local Constitutive Behavior and Simulation on Tensile Test of 2219-T87 Aluminum Alloy GTAW Joints. *Trans. Nonferrous Met. Soc. China* **2015**, *25*, 3072–3079. [[CrossRef](#)]
48. Bai, Y.; Wierzbicki, T. Application of Extended Mohr-Coulomb Criterion to Ductile Fracture. *Int. J. Fract.* **2010**, *161*, 1–20. [[CrossRef](#)]
49. Bao, Y.; Wierzbicki, T. On Fracture Locus in the Equivalent Strain and Stress Triaxiality Space. *Int. J. Mech. Sci.* **2004**, *46*, 81–98. [[CrossRef](#)]
50. Bao, Y.; Wierzbicki, T. On the Cut-off Value of Negative Triaxiality for Fracture. *Eng. Fract. Mech.* **2005**, *72*, 1049–1069. [[CrossRef](#)]

51. Jenkins, W.D.; Willard, W.A. Effect of Temperature and Notch Geometry on the Tensile Behavior of a Titanium Alloy. *J. Res. Natl. Bur. Stand. Sect. C Eng. Instrum.* **1966**, *70*, 5–11. [[CrossRef](#)]
52. Kumar, J.G.; Nandagopal, M.; Parameswaran, P.; Laha, K.; Mathew, M.D. Effect of Notch Root Radius on Tensile Behaviour of 316L(N) Stainless Steel. *Mater. High Temp.* **2014**, *31*, 239–248. [[CrossRef](#)]
53. Lei, X.; Li, C.; Shi, X.; Xu, X.; Wei, Y. Notch Strengthening or Weakening Governed by Transition of Shear Failure to Normal Mode Fracture. *Sci. Rep.* **2015**, *5*, 10537. [[CrossRef](#)]

Disclaimer/Publisher’s Note: The statements, opinions and data contained in all publications are solely those of the individual author(s) and contributor(s) and not of MDPI and/or the editor(s). MDPI and/or the editor(s) disclaim responsibility for any injury to people or property resulting from any ideas, methods, instructions or products referred to in the content.